



Cite this: *New J. Chem.*, 2023, 47, 4897

Synthesis of a novel perovskite-carbon aerogel hybrid adsorbent with multiple metal-Lewis active sites for the removal of dyes from water: experimental and DFT studies†

Daryoush Sanaei,^a Mohammad Hadi Dehghani,^{b,c} Hamidreza Sharifan,^d Monika Jain,^e Bahram Roshan,^a Javier A. Arcibar-Orozco^f and Vassilis J. Inglezakis^g

Mixed perovskites have vast industrial potential, but some challenges (*i.e.*, aggregation and chemical instability) limit their applications. Herein, a novel environment-friendly carbon aerogel (CAG) synthesized from sodium alginate (SA) was used as a precursor to create a double-B-site perovskite/carbon aerogel hybrid adsorbent (($\text{Sr}_{0.7}\text{Mn}_{0.3}\text{Co}_{0.5}\text{Fe}_{0.5}\text{O}_{3-\delta}$)/CAG) (DB-perovskite/CAG hybrid). The adsorbent was extensively characterized via different techniques, including X-ray photoelectron spectroscopy and Fourier transform infrared (FTIR) spectroscopy. The removal efficiency for crystal violet (CV) and acid yellow 17 (AY17) was conducted over various pH, adsorbent/adsorbate dosages, and reaction times in an aqueous system. The maximum adsorbed concentration (Q_{max}) recorded by 206 mg g^{-1} and 113 mg g^{-1} for CV and AY17, respectively, and compared to the performance of only DB-perovskite (114 mg g^{-1} and 59 mg g^{-1}), respectively. The adsorption site energy distribution was studied by applying the density functional theory (DFT). The adsorption on the DB-perovskite/CAG hybrid was significantly regulated by pH change. The cooperative metal active/Lewis acid sites of the DB-perovskite/CAG adsorbent led to a faster and higher adsorption capacity toward CV and AY 17. The doping of Mn indicated a synergistic effect in improving the adsorption of either dye through the introduction of abundant active sites and strengthening of metal-functional groups ($-\text{C}-\text{O}-\text{C}$, $-\text{COOH}$, and $\text{C}-\text{OH}/\text{O}-\text{H}$)– π aromatic bonding, confirmed by DFT calculations.

Received 17th November 2022,
Accepted 16th January 2023

DOI: 10.1039/d2nj05646a

rsc.li/njc

Introduction

The removal of organic dyes from industrial wastewater has been a challenging issue since they are highly toxic, with an annual production rate of 700 000 metric tons.^{1,2} A variety of industries, such as cosmetics, paint, paper, and textile, release

a significant amount of dyes into wastewater annually. Textile industries are the primary source of dye pollution, with over 140 000 tons of annual discharged dyes worldwide.^{3,4} Dye treatment and removal primarily depend on the physiochemical properties of dyes. The two types of dyes that have been frequently reported due to removal challenge, persistency, and high health risk in the aqueous systems are acid yellow 17 (AY 17), a monoazo dye (disodium 2,5-dichloro-4-[5-hydroxy-3-methyl-4-(sulphophenylazo)pyrazol-1-yl] benzenesulphonate), and crystal violet (CV), a triarylmethane dye (hexamethyl pararosaniline chloride).⁵ Inefficient treatment of dyes from wastewater leads to the build-up of a toxic concentration of organic dyes, which causes respiratory problems, genotoxicity, cytotoxicity, and carcinogenicity.⁶ Due to the photostability, thermal resistance, and poor biodegradability nature of organic dyes,¹ low-cost, renewable, and efficient treatment techniques are in high demand. Conventional wastewater treatment processes often fail to efficiently remove dyes and their by-products from effluents.⁷ Among the numerous proposed dye removal techniques, adsorption has demonstrated promising applications due

^a Department of Environmental Health Engineering, Faculty of Public Health and Safety, Shahid Beheshti University of Medical Sciences, Tehran, Iran

^b Department of Environmental Health Engineering, School of Public Health, Tehran University of Medical Sciences, Tehran, Iran

^c Institute for Environmental Research, Center for Solid Waste Research, Tehran University of Medical Sciences, Tehran, Iran

^d Department of Natural Science, Albany State University, Georgia, USA

^e Department of Natural Resource Management, College of Forestry, Banda University of Agriculture and Technology, Banda, India

^f Research Department, CIATEC A.C. Centro de Innovación Aplicada en Tecnologías Competitivas, León, Mexico

^g Department of Chemical & Process Engineering, University of Strathclyde, Glasgow, UK. E-mail: vassileios.inglezakis@strath.ac.uk

† Electronic supplementary information (ESI) available. See DOI: <https://doi.org/10.1039/d2nj05646a>



to its high potential to remove dyes with different physiochemical properties from an aqueous system.

As a class of widespread natural materials, perovskites have attracted considerable attention due to their unique properties, such as abundant active sites, high chemical and thermal durability, and tunable structure. Researchers reported the broad applicability of perovskite nanomaterials from catalysis to the adsorption process due to their excellent optical, magnetic, thermal, and electric characteristics.^{8,9} The high adsorption capacity and fast kinetics of perovskites make them suitable adsorbent candidates in industrial wastewater bearing high levels of organic dyes.^{10–12} For instance, Cuijin Pei *et al.* 2016 showed a remarkable adsorption capacity (7154 mg g^{−1} in 40 min) for Acid Fuschia (AF) using a 3-dimensional hierarchical ZnO adsorbent.¹³ Perovskites are ceramic materials with the formula of ABO₃, classified as metal oxides. Cationic sites of A and B are commonly alkaline-earth/rare-earth metals and transition metals with partially filled d-orbitals, respectively. The redox reactions usually occur at the B-site, which plays a primary role in pollutant removal. Several researchers reported that these perovskite nanomaterials could be used in many applications from catalysis to adsorption process due to good optical, magnetic, thermal, and electric characteristics.^{8,9,14} Several synthetic methods have been reported for preparing perovskites that included sol-gel, Pechini, co-precipitation, chelating complex, and pyrolysis.^{15–18} The perovskites exhibit not only higher adsorption capacity and fast kinetics but also act as suitable adsorbents toward industrial wastewater with high concentration.^{10–13} Moreover, the perovskites contain a larger number of active sites than that of conventional materials.^{19–21} However, B-site perovskite suffers from slow electron transfer, low electrical conductivity, and poor and unstable active sites. Therefore, engineering modification of B-sites with appropriate substitution can enhance perovskite adsorption capacity. For example, the B-site of cobalt-doped perovskite oxide (BaCo_xNi_{1−x}O_{3−δ}) significantly increased the oxygen adsorption capacity by 49.5 mg g^{−1}.²² H. Sun *et al.* 2017 reported outstanding oxygen evolution reaction (OER) electrocatalyst of a double-B-site perovskite oxide compared with those of single perovskite oxides.²³ However, the literature is minimal on dual-B site perovskites as adsorbents for persistent organic pollutants, particularly cationic and anionic dyes.

To optimize the double-B-site performance, a novel integration of the chemical properties of several key elements is of high interest. This study formulated a hybrid adsorbent on carbon-based support to improve the stability and homogenous dispersion of double-B-sites (DB) perovskite. Carbon Aerogel (CAG) with a nanoporous structure provides support with excellent porosity, high specific surface area, and conductivity. Also, it reinforces the overall thermal and mechanical stability of the perovskite. The hybrid would further lead to great treatment efficiency in a cost-effective manner for the purification of effluents/wastewater. CAG has been investigated as an adsorbent for several pollutants such as inorganic (especially metal ions), pharmaceuticals, and various gases; also, its used for the removal of organic dyes has been widely reported (R).

This environment-friendly hybrid adsorbent would prevent the aggregation of nanoparticles owing to high porosity and large surface area. To the best of our knowledge, this is the first report on the synthesis of DB-perovskite/CAG hybrid (Sr_{0.7}Mn_{0.3}Co_{0.5}Fe_{0.5}O_{3−δ}/CAG). This study aims to evaluate the efficiency, application, and durability of a DB-perovskite/CAG hybrid for the removal of two commercial dyes of CV and AY 17 from an aqueous system. The relationship between the functionality and composition of the DB-perovskite/CAG was investigated through extensive material characterization such as X-ray photoelectron spectroscopy (XPS) and density functional theory (DFT) calculations. The designed hybrid adsorbent exhibits the advantage of single perovskite with mixed oxidation states of Fe, Co, and Mn, and those of the double B-site perovskite with arranged and multi-active sites for enhancing the adsorption of CV and AY17 molecules in aqueous solution. This study provides a baseline for applying novel hybrid perovskites and removing dyes with various physiochemical properties.

Materials and methods

Reagents

Iron(III) nitrate nano hydrate (Fe(NO₃)₃·9H₂O, ACS reagent ≥ 98%), manganese(II) nitrate tetrahydrate (Mn(NO₃)₂·4H₂O, ≥ 97.0% (KT)), strontium nitrate (Sr(NO₃)₂, 99.995% trace metals basis), cobalt(II) nitrate hexahydrate (Co(NO₃)₂·6H₂O, ACS reagent, ≥ 98%), citric acid (C₆H₈O₇), and ethylenediaminetetraacetic acid (EDTA) were purchased from Fisher Scientific Company, USA. Formaldehyde solution (HCOH, 37%) and resorcinol (C₆H₄(OH)₂, 99.9%) were obtained from Merck Millipore. Crystal violet (C₂₅H₃₀ClN₃, C.I. 42555), Acid Yellow 17 (C₁₆H₁₀C₁₂N₄Na₂O₇S₂, dye content 60%), and sodium alginate were supplied by Sigma Aldrich, USA. Anhydrous calcium chloride was bought from Aladdin Chemical Reagent Co. Ltd (Shanghai, China).

Preparation of environment-friendly carbon aerogel (CAG)

To prepare the carbon aerogel (CAG), 1 g sodium alginate (SA) was added to 50 mL distilled H₂O to produce a viscous solution, followed by stirring at 45 °C for 30 min. The SA solution was slowly dropped into 200 mL 2.5 wt%. CaCl₂ solution under magnetic stirring using a 5 mL syringe. After 1 h, the dispersed granular hydrogel was transferred to a 0.2% CaCl₂ solution to promote solidification. The resulting SA hydrogel was washed with distilled water and 96% ethanol to remove any impurities and unbound CaCl₂ from the surface. Subsequently, the prepared hydrogel was frozen in a −80 °C for 2 h. To form SA aerogel from SA hydrogel, the vacuum freeze-dryer technology (FD-1-50, Boyikang Laboratory Apparatus Co., Ltd, Beijing, China) was used. The resulting aerogel was heated in a tube furnace (GSL-1700X, MTI Corporation, USA) for 30 min at 800 °C under nitrogen atmosphere with a 10 °C min^{−1} as the heating rate to form the SA-based carbon aerogel.

Preparation of double-B-site perovskite

The double-B-site perovskite (Sr_{0.7}Mn_{0.3}Co_{0.5}Fe_{0.5}O_{3−δ}) was synthesized by the modified Pechini method known as the



EDTA-CA-complexing sol-gel.^{24–26} Briefly, 3.7 g Sr, 1.88 g Mn, 5.05 g Fe, and 3.63 g Co were dissolved in 25 mL deionized water. Next, citric acid and ethylene diamine tetra-acetic acid (EDTA) as the complexing agents were added to the solution with a molar ratio of citric acid/EDTA/total metal ions of 1.2:1:1. pH was adjusted to 6.5 by the dropwise addition of ammonia solution (25 wt%). The mixed solution was vigorously shaken at 95 °C for 3 h (Heidolph Instruments, Unimax 2010) to form a transparent gel that was dried in an oven overnight. The dried gel was thermally treated in two steps first, pre-calcination at 450 °C for 8 h, and calcination at 800 °C for 7 h. The double-B-site perovskite ($\text{Sr}_{0.7}\text{Mn}_{0.3}\text{Co}_{0.5}\text{Fe}_{0.5}\text{O}_{3-\delta}$) was kept in a desiccator for further experiments and characterization. The flow diagram of preparation is depicted in the (ESI†).

Preparation of the DB-perovskite/CAG hybrid

For DB-perovskite/CAG hybrid synthesis, 1.22 g CAG and 0.5 g perovskite were mixed for 30 min. Then, 140 mL sodium hydroxide (1.5 M) was added to the prepared solution for 60 min under vigorous stirring at room temperature for 24 h. After that, 100 mL sodium hydroxide (3 M) was added to the solution for another 4 h. The obtained DB-perovskite ($\text{Sr}_{0.7}\text{Mn}_{0.3}\text{Co}_{0.5}\text{Fe}_{0.5}\text{O}_{3-\delta}$)/CAG was vacuum filtered and washed several times with distilled water to achieve the pH of 7–8 and dried in an oven overnight. The resulting powder was heated in a tube furnace (GSL-1700X, MTI Corporation, USA) for 1 h at 800 °C under a heating rate of 10 °C min⁻¹ at a nitrogen flow of 120 cm³ min⁻¹.

Characterization of the perovskite

The perovskite was extensively characterized by X-ray photoelectron spectroscopy (XPS) using an Omicron ESCA 250 (Scienta Omicron GmbH, Germany) using monochromatic Al K α (1486.6 eV). The composition was analyzed at 225 W, passing an energy of 100 eV (survey scans) and 50 eV (specific regions). A Gaussian function fitted the peaks using the Origin software 2017 (OriginLab, Northampton, MA). In addition, FT-IR spectroscopy quantified the bonding arrangements within 4000 to 400 cm⁻¹ (Thermo Scientific; model Nicolet iS10). The N₂ adsorption-desorption isotherms were applied to estimate the specific surface area (S_{BET}), total pore volume (V_t), and pore size distributions (ASAP 2020 M, Micromeritics Inc., USA).

Experimental design

The adsorption of two cationic dyes of crystal violet (CV) and acid yellow 17 (AY17) onto the DB-perovskite/CAG hybrid was performed in batch reactors. Briefly, different doses of the adsorbent (0.005 g to 0.05 g for CV and 0.02 g to 0.14 g for AY17) were added in Erlenmeyer flasks containing different concentrations of CV and AY17 (5 to 40 mg L⁻¹) in duplicate. In each series of experiments, a control was used without the addition of the adsorbent (only dye). The flasks were shaken at 180 rpm for 1 h. Right after this, the adsorbent in each flask was separated by a membrane filter syringe (0.45 microns), and the concentration of dyes in the supernatant was measured by a UV-Vis spectrophotometer ($\lambda_{\text{max}} = 590$ nm for CV and $\lambda_{\text{max}} = 402$ nm for AY17). The adsorption capacity of CV and AY17 was calculated using eqn (1).^{27–29}

$$q_e = q_t = \frac{(c_0 - c_{e,t})V}{m} \quad (1)$$

where C_{00} and C_e (mg L⁻¹) refer to CV or AY17 concentration at time zero and the equilibrium state, respectively, m (g) indicates the mass of perovskite/CAG, and V (L) refers to the volume of the CV or AY17 solution. The kinetic (pseudo-first order, pseudo-second order, and Elovich) and isotherm models (Langmuir, Freundlich, Temkin, and D-R models) were applied to understand the dye adsorption mechanism. Moreover, to investigate the rate-determining steps for the kinetics of adsorption, the intraparticle diffusion, Bangham, and Boyd models were studied. The affinity of the DB-perovskite/CAG for the adsorption of CV and AY17 was obtained by measuring the distribution coefficient (K_d) that was calculated from the experimental data of various initial concentrations (C_0) using eqn (2).

$$K_d = \frac{(C_0 - C_q)V}{C_q m} = \frac{Q_q}{C_q} \quad (2)$$

where V was the solution volume, C_q was the equilibrium concentration, and m was the mass of the DB-perovskite/CAG hybrid.

Results and discussion

Structural and morphological characterization

XPS analysis. The XPS spectra of the DB-perovskite/CAG hybrid adsorbent is shown in Fig. 1A and the corresponding high-resolution XPS spectra of C 1s region of the DB-perovskite/CAG

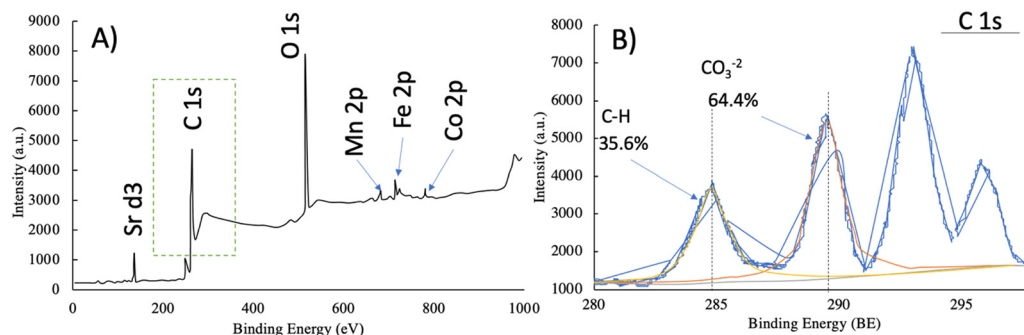


Fig. 1 (A) The full spectrum of the DB-perovskite/CAG hybrid obtained from XPS analysis; (B) C 1s XPS spectra of the DB-perovskite/CAG hybrid.



hybrid in Fig. 1B. The C 1s spectrum can be steadily deconvoluted into three prominent Gaussian peaks at 283.8, 286.6, and 288.1 eV. The peak at lower binding energy (283.8 eV) is ascribed to the C valence state present in CAg, while the peak at 586.6 eV is assigned to the oxygen vacancies and defects in the mixed perovskite. The main peak at binding energy (BE) 283.8 eV represents the CHx, C-C, and C=C groups of aliphatic and aromatic structures. The two peaks at BE of 286.6 eV and 288.1 eV denote C=O in ketone and carbonyl and O-C=O in carboxylic groups, respectively. The peak at a binding energy of 289.6 eV signifies plasmon losses or shake-up peak of π - π^* bonding stemming from π -electrons in aromatic rings.³⁰ The surface characteristics (relative concentration) of the adsorbent hybrid calculated from the XPS spectra is provided in Table S1 (ESI†).

FTIR and FE-SEM analysis. Fig. 2a shows the FTIR spectra of the DB-perovskite/CAg hybrid adsorbent. The intense peaks in the region of 3434.24 cm^{-1} and 3752.4 cm^{-1} in CAg can be ascribed to bulk O-H groups in the hydrate, phenols, and carboxylic groups and also moisture due to the hygroscopicity of CAg.³¹ It was suggested that the OH groups in CAg are dominantly present as free OH that reacted with metal oxides. Therefore, there was a high potential for AY17 and CV adsorption through unpaired electrons and hydrogen bonding. Also, the other functional groups on the surface of carbon aerogel (CAg) and DB-perovskite/CAg hybrid are $1628\text{ and }1726\text{ cm}^{-1}$ (C=O in the carboxylic, ester, and lactonic groups); $1389\text{ and }1102\text{ cm}^{-1}$ (C-O stretch in secondary alcohol). The peak at 1108.6 cm^{-1} pertains to three-dimensional M-O-M stretching vibrations. Peaks at $574\text{ and }860\text{ cm}^{-1}$ correspond to the formation of M-O bonds originated by the intrinsic nature of vibrations at tetrahedral places of the metal. The spectra

suggested the presence of active sites on the adsorbent surface. The sharp peak observed at 1452 cm^{-1} only in the DB-perovskite/CAg hybrid but not in the CAg spectra signifies the bending vibration of hydroxyl groups on the surface of $\text{Sr}_{0.7}\text{Mn}_{0.3}\text{Co}_{0.5}\text{Fe}_{0.5}\text{O}_{3-\delta}$ (M-OH). The peak position and also intensities were shifted, implying an interaction between the surface OH groups with both AY17 and CV after adsorption. Moreover, the formation of new bands ($574\text{ and }860\text{ cm}^{-1}$) in lower frequencies supported the adsorption of CV and AY17 through ion-exchange interactions.^{32–34} The morphology and microstructure of the as-prepared adsorbent are depicted by SEM analysis (Fig. 2b). Alginate that comprised D-mannuronate (M) and α -L-guluronate (G) monomers can be used as a precursor to prepare a carbon aerogel by dispersing wet spun sodium alginate into a coagulating bath of 2.5 wt%. CaCl_2 aqueous solution. Calcium cations can induce an interchain between the long structure of G-units and gel junction zones, whose structure has been known as an egg-box structure. After drying and converting it to aerogel, it is carbonized at high temperature in N_2 atmosphere to prepare carbon aerogel nanocomposite or sheet, wherein the DB-perovskite nanoparticles can be encapsulated or distributed well by the carbonized alginate. As can be seen, the well distributed DB-perovskite over CAg and also the presence of a rough surface can enhance the contact active area between the DB-perovskite/CAg hybrid and dyes in aqueous solution and also provide extra binding sites, which is beneficial for the quick adsorption of the target dye molecules and further enhancing the adsorption capacity of the DB-perovskite/CAg hybrid for dye molecules.

Adsorption behavior. As shown in Table 1 and Fig. 3a, the K_d value of the DB-perovskite/CAg hybrid was higher for CV than

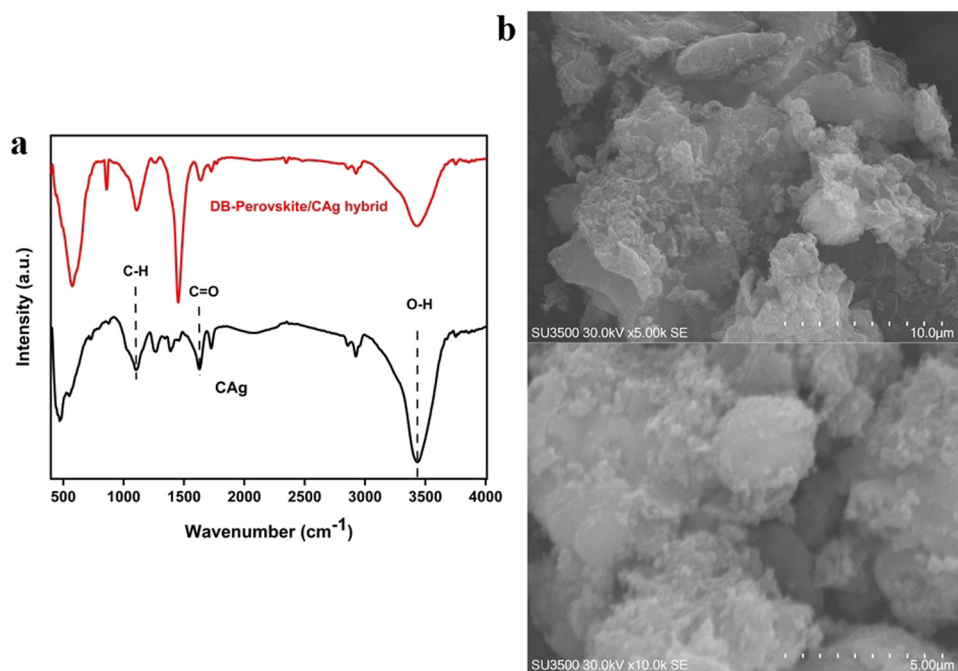


Fig. 2 (a) FTIR plot of Carbon Aerogel (CAg) and DB-perovskite/CAg hybrid obtained at 4 cm^{-1} resolution averaging 128 scans, purged with helium gas; and (b) SEM images of the as-prepared DB-perovskite/CAg hybrid.



Table 1 Comparison of the adsorption affinity of different adsorbents with DB-perovskite/CAG hybrid adsorbent for the removal of dyes from the aqueous phase

Type of adsorbent	Type of pollutants	Selectivity coefficient (mL g ⁻¹)	Ref.
DB-perovskite/CAG hybrid	CV	985	This study
	AY17	440	This study
Fuller's earth (FE) ^a	Methylene blue (MB)	600	1
Activated carbon	Rhodamine B	302	2
MCM-41 ^b	Rhodamine B	56.2	2
TM	Rhodamine B	31.7	2
Bulk Fe ₂ O ₃	Rhodamine B	177	2
Activated carbon ^c	Sudan dye(III)	120	3
Bamboo biochar	Red 46 dye	600	4
Rice straw biochar	Red 46 dye	245	4
UiO-66	Methyl orange	1025	5
UiO-66	Malachite green	225	5

^a Adsorptive removal of methylene blue from colored effluents on Fuller's earth. ^b Low-spin-state hematite with superior adsorption of anionic contaminations for water purification. ^c Adsorption of the Sudan dye(III) in methanol using activated carbon.

AY17 under an initial concentration of 50 mg L⁻¹, indicating that the DB-perovskite/CAG hybrid is considered to be an excellent adsorbent for CV. The K_d value of Sr_{0.7}Mn_{0.3}Co_{0.5}Fe_{0.5}O_{3-δ}/CAG was higher in comparison to other adsorbents in the literature.^{7,35–40} It was found that the DB-perovskite/CAG hybrid leads to a higher K_d than other adsorbents, suggesting higher retention and low mobility of CV and AY17 in an aqueous solution. The CV molecules have smaller sizes than AY17. Therefore, their mobility through the cavity of DB-perovskite/CAG hybrid is relatively faster (Fig. 3b). Hence, it leads to enhanced adsorption activity than that AY17.

The key parameters affecting adsorption performance. Regarding the removal of CV, the adsorption rate was faster, reaching equilibrium after 15 min. For the AY17 (Fig. 3c and d), the adsorption rate slowly increased and reached equilibrium within 60 min. As illustrated in Fig. 3c and d, for removing CV, when the dosage was increased from 0.005 g to 0.05 g/50 mL, CV removal increased step-wise by 41%, 63%, 95%, and 98%, respectively. In contrast, by increasing DB-perovskite/CAG hybrid concentration from 0.02 to 0.14 g/50 mL, the removal of AY17 increased from 74% to 93.5% at 0.1 g and it then gradually decreased to 91% at 0.14 g/50 mL. The higher DB-perovskite/CAG dose likely corresponds to pH-dependent adsorption mechanisms. Moreover, as the initial concentration and volume of dyes are constant, the number of contacted and adsorbed dye molecules or ions by the DB-perovskite/CAG Hybrid per unit mass decreases as the adsorbent dosage increases, and the active sites of DB-perovskite/CAG Hybrid are not fully occupied.

Overall, the DB-perovskite/CAG hybrid is highly sustainable compared to other pH-sensitive adsorbents. For instance, for tea leaves modified with polyethyleneimine (PEI-STL),^{41,42} efficient adsorption took place at pH 3 and for the almond shell,⁴³ the optimal removal of cationic dyes occurred at pH 8–10. More details about the influence of the experimental conditions on the removal performance are presented in Fig. S1 (ESI†).

Adsorption isotherm and kinetics evaluation. The adsorption isotherm models fitted by Langmuir, Freundlich, Temkin, and DR are shown in Fig. 4a (also Fig. S2 and Table S2, ESI†). The interaction between CV and DB-perovskite/CAG hybrid surface was better elucidated by the Langmuir model (Fig. 4a). It represents monolayer adsorption, suggesting the monolayer

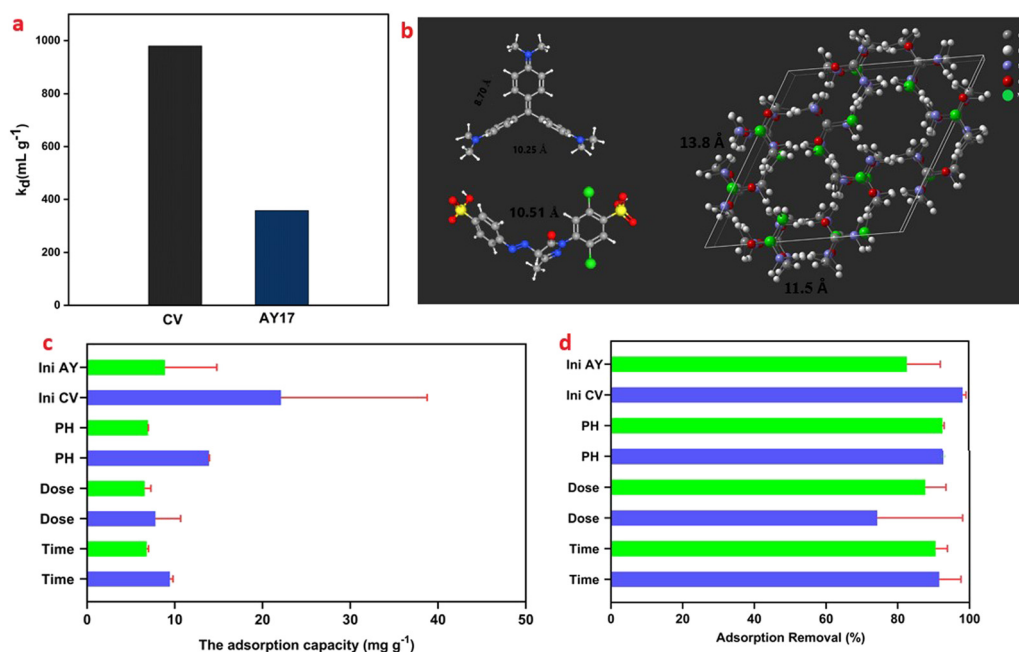


Fig. 3 (a) Adsorption coefficient (K_d) values for the adsorption of CV and AY17 on DB-perovskite/CAG hybrid; (b) the size of the AY17 and CV molecules in comparison with pore sizes of DB-perovskite/CAG hybrid composite; and the main parameters affecting the adsorption process in terms of (c) adsorption capacity and (d) adsorption removal.



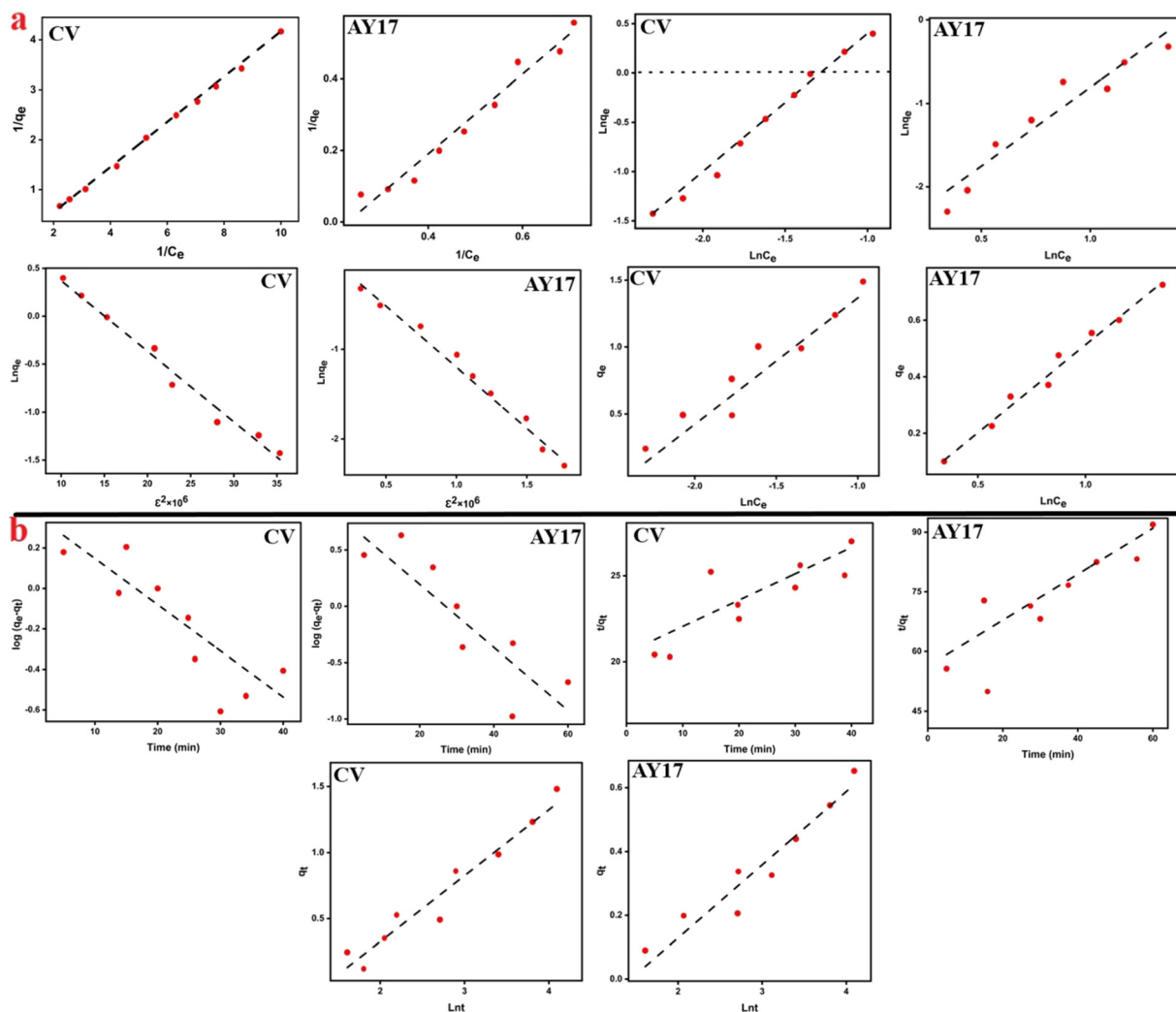


Fig. 4 The adsorption isotherms fitted with (a) Langmuir, Freundlich, D–R, and Temkin models, respectively; and kinetics (b) pseudo-first order, pseudo-second order, and Elovich models, respectively (experimental condition: pH (neutral); agitation speed (210 rpm); adsorbent dosage (0.1 g for AY17 and 0.05 g for CV; contact time (10 min for CV and 60 min for AY17); initial dye concentration (5–40 mg L⁻¹); volume of reaction (V = 50 mL); and temperature (25 °C)).

coverage of dye molecules on a homogenous adsorbent surface with the same and equivalent adsorption active sites. While the Dubinin–Radushkevich (D–R) and Temkin models are based on the higher R^2 and lower ARE, χ^2 and Δq were fitted better for the adsorption of AY17 on DB-perovskite/CAG hybrid (Fig. 4a). For the adsorption of CV and AY17, the maximum adsorption capacity (Q_{\max}) was 206 mg g⁻¹ and 113.54 mg g⁻¹, respectively, compared to solely DB-perovskite (114 mg g⁻¹ and 59 mg g⁻¹, respectively).

The kinetics results of DB-perovskite/CAG hybrid on the adsorption of dyes are shown in Fig. 4b and Table S3 (ESI†). It can be seen that the adsorption capacity (q_e) of AY17 was 26.11 mg g⁻¹, which is smaller than that for CV (29.55 mg g⁻¹) in the pseudo-first order model. The results indicated that the adsorption data fitted better with the Elovich model based on coefficient (R^2) and lower error analysis (ARE, χ^2 , and Δq) than pseudo-first order and pseudo-second order kinetics. This result was based on the higher correlation coefficient (R^2) and

lower error analysis (ARE, χ^2 , and Δq) values than pseudo-first and pseudo-second order models (Table S3, ESI†). The Elovich model assumes that the entire adsorbent surface is highly heterogeneous. As the initial concentration is increased, the parameter α would increase and constant β would decrease.⁴⁴ The constant β is related to the extent of surface coverage, increasing the reaction rate of adsorption as the initial concentration decreases, which might be related to the expansion of the available sites for the adsorbate.

Rate-determining mechanism for adsorption

Boyd's film diffusion model. The first step in the adsorption process is the transport of dye molecules within the pores of the DB-perovskite/CAG hybrid. A linear or non-linear plot was obtained by plotting the graph between B_t vs. t (min), called the Boyd plot. If the graph passes through the origin or not-origin, then the adsorption process is controlled by intraparticle diffusion only or both film and intraparticle resistance, respectively.



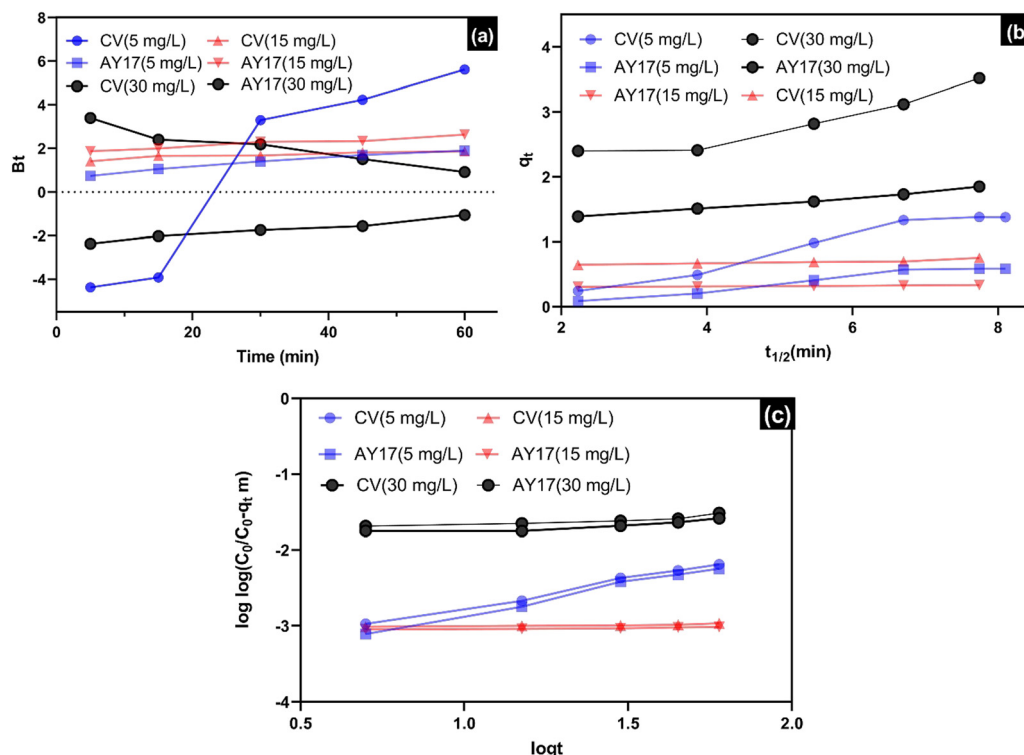


Fig. 5 (a) Boyd model; (b) intraparticle diffusion, and (c) Bangham model for the adsorption of CV and AY17 on the DB-perovskite/CAG hybrid at 303.15 K.

The Boyd plot was obtained at different concentrations, as depicted in Fig. 5a. The plot at the lower initial concentration (5 mg L^{-1}) is completely non-linear and does not pass through the origin for CV, while it is linear and passed through the origin for the AY 17. The pattern suggested that the adsorption of CV onto DB-perovskite/CAG hybrid is mainly controlled by film diffusion and intraparticle resistance, whereas in AY 17, it is controlled by film diffusion. However, the plot appeared linear when the initial concentration was increased for both CV and AY17. However, the plot for CV at higher concentrations became non-linear. Overall, it was concluded that the adsorption process for CV is controlled by both film and intraparticle resistance, while the film diffusion is dominated by diffusion mechanisms for AY17 adsorption.

Intraparticle diffusion model. The intraparticle diffusion model developed by Weber and Morris and McKay and Poots, calculating diffusion rate from the plots of q_t vs. $t^{1/2}$ (Fig. 5b), is depicted by the following eqn (3).^{45,46}

$$q_t = k_{id}t^{1/2} + C \quad (3)$$

where K_{id} is the intraparticle kinetic parameter that was obtained from the slope of the plot. The plot is multilinear in nature showing several steps taking place: the first portion of the plot is related to external diffusion; the second portion explains gradual diffusion of dyes into the pore, indicating that diffusion is the rate-limiting step; the last part is related to equilibrium adsorption. The intraparticle diffusion rate (k_{int}) increased with the initial concentration of the dyes. Then, it

describes the growing impact of the driving force, signifying the reduction in the diffusion of dyes in the boundary layer and increasing the diffusion of dyes in the adsorbent. As shown in Fig. 5b, at different concentrations of CV and AY 17, the fitted curve consisted of two fitted segments for CV, the first one exhibiting boundary diffusion and another one directing intraparticle diffusion. It could be interpreted that the adsorption of CV by DB-perovskite/CAG hybrid adsorbent increased linearly from boundary (external) diffusion to intraparticle diffusion until complete saturation of DB-perovskite/CAG hybrid with CV (final curved portion) under equilibrium conditions. On the other hand, there was only one portion of fitted line for AY17, implying that the adsorption of AY 17 by the DB-perovskite/CAG hybrid could not reach equilibrium as AY17 needed more time than CV to reach the equilibrium state, according to physico-chemical analysis. Moreover, to carry out the intraparticle transport of dye molecules through the pores of DB-perovskite/CAG hybrid particles, the diffusion constant is calculated by applying eqn (4) and (5).

$$D_i = \frac{0.03 \times r^2}{t_{1/2}} \quad (4)$$

$$t_{1/2} = \frac{1}{kd_e} \quad (5)$$

where D_i is the diffusion coefficient ($\text{cm}^2 \text{ s}^{-1}$), and r is the average radius of adsorbent (cm). The value of r was calculated as $67 \times 10^{-4} \text{ cm}$ by assuming spherical shape of the adsorbent particles.



The value of D_i increased from 1.53×10^{-5} to $9.52 \times 10^{-5} \text{ cm}^2 \text{ s}^{-1}$ for CV and 3.31×10^{-6} to $2.39 \times 10^{-5} \text{ cm}^2 \text{ s}^{-1}$ for AY17 with an increase in the initial concentration of the dyes from 5 to 30 mg L^{-1} .^{47–49} In this study, the values of R^2 and error analysis (Table S4, ESI†) were estimated from the Boyd model. (Film diffusion) was less than intraparticle diffusion, suggesting both the models occurred simultaneously, but intraparticle diffusion model was the dominant rate-determining step.

Bingham's model. Bingham's model was applied to understand the rate-controlling step in the adsorption process (Fig. 5c). The Bingham model showed limited adsorption kinetics with pore diffusion. It was observed that the α decreased from 0.305 to 0.18 for CV and from 0.368 to 0.179 for AY17, and the k_0 values increased from 11.19 to $22.21 \text{ mL g}^{-1} \text{ L}^{-1}$ for CV and from 11.19 to $19.99 \text{ mL g}^{-1} \text{ L}^{-1}$ for AY17, when the initial concentration of the dyes was increased. This change confirmed that the pore diffusion of CV and AY17 molecules drives the adsorption process by $\text{Sr}_{0.7}\text{Mn}_{0.3}\text{Co}_{0.5}\text{Fe}_{0.5}\text{O}_{3-\delta}$. For choosing the best kinetic model and adsorption mechanism, generally, correlation coefficient (R^2) is not the only appropriate criterion. Thus, for comparison of models, three error analysis (Δq %, ARE, and χ^2) (eqn (6)–(8)) Table S4, ESI†) was done. The results showed that the correlation coefficient and error parameters for the intraparticle diffusion and Bingham's models for both the dyes (AY17 and CV) fitted better than the other models. According to higher R^2 value and error analysis for the intraparticle and Bingham's curves, the diffusion of CV and AY 17 into the internal pores of the DB-perovskite/CAG hybrid was considered as the slowest step in the adsorption mechanism. As a result, various mechanisms translate the kinetic adsorption of CV and AY17 on the DB-perovskite/CAG hybrid. On the other hand, adsorption process is a heterogeneous process that happened at the liquid–solid boundary for AY17 and the mixing of pore diffusion and film (intraparticle) diffusion for both the dyes, called as “complex mechanisms”.^{50–52} However, for describing the satisfactory implementation of the kinetics/equilibrium models, a rough estimation of solid phase diffusion coefficients is acceptable, and equilibrium constants and conclusions on the underlying mechanisms should be treated with caution.^{53,54}

$$\Delta q(\%) = 100 \times \sqrt{\frac{\left\{ \frac{q_{t,\text{exp}} - q_{t,\text{cal}}}{q_{t,\text{exp}}} \right\}^2}{n - 1}} \quad (6)$$

$$\chi^2 = \sum_i^N \frac{(q_{e,\text{exp}} - q_{e,\text{cal}})^2}{q_{e,\text{cal}}} \quad (7)$$

$$\text{ARE} = \sum_{i=1}^N \left| \frac{(q_{e,\text{exp}} - q_{e,\text{cal}})}{q_{e,\text{exp}}} \right| \quad (8)$$

where N is the number of tested experiments in the dye's adsorption, and the subscripts “exp” and “cal” indicate experimental and calculated parameters, respectively.

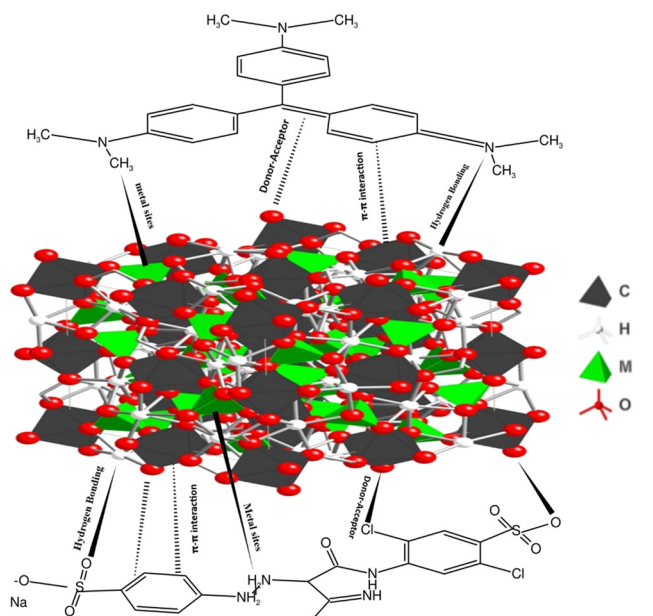


Fig. 6 The potential interactions driving dye adsorption on the DB-perovskite/CAG hybrid at wide ranges of pH, including electrostatic attachment and hydrogen bonding.

The adsorption behavior at different pH. The adsorption potential of the DB-perovskite/CAG hybrid for the removal of both dyes is illustrated in Fig. 6 at two different pH values. The DB-perovskite/CAG hybrid is an effective material to treat dye laden wastewater under acidic, neutral, and weak alkaline conditions. As can be explained, the adsorption of CV on the DB-perovskite/CAG hybrid was not significantly affected by pH. At higher pH, the adsorption of CV was slightly decreased. The pH may affect the adsorption by multifarious electrostatic interaction, electrophilic–nucleophilic interactions, hydrogen bonding, and proton transfer reaction. In the acidic condition, all three N atoms in CV can be fully protonated, sparking the interaction with the negatively charged surface (OH, carboxylic acid, and oxygen) of the DB-perovskite/CAG hybrid.⁵⁵ When pH becomes alkaline, the interaction between CV and DB-perovskite/CAG hybrid is dominated by electrophilic–nucleophilic (Lewis's acid–base reaction) mechanism. The introduction of DB-perovskite into the porous networks of CAG creates additional metal–active sites. Moreover, the DB-perovskite can directly bind with the inner atoms of CAG such as N and O, providing M–O or M–N/C bond (M = Fe, Co, Mn) that can serve as the active sites for the adsorption of CV. Such active sites consist of a cloud of electrons of the Sigma band. As a result of this cloud of electrons, the DB-perovskite/CAG hybrid can be considered as nucleophilic. The nucleophilic DB-perovskite/CAG hybrid interacts with electrophilic central carbon/nitrogen of CV. Under weak alkaline conditions (pH = 8.5), the relative content of OH ions as the nucleophile is less competitive with the proposed nucleophile (DB-perovskite/CAG hybrid). However, the adsorption efficiency decreases at higher pH, which allows to predict a more decreasing rate at alkaline pH with increasing OH ions.^{56,57}

The introduction of DB-perovskite into the porous structure of CAG can create various surface functional groups from basic



groups to acidic groups and active metal sites. The electrostatic interactions between AY 17 and DB-perovskite/CAG hybrid were considered major mechanisms related to pH in the adsorption process.^{58,59} However, pH changes in the solution might create changes in the AY17 structure and adsorption mechanisms by the DB-perovskite/CAG hybrid. At solution pH lower than the pK_a of AY17 (5.5),^{60–63} the AY 17 dye exists primarily in its acidic form; as a result, the relatively negatively charged surface of the DB-perovskite/CAG hybrid can adsorb AY 17 with a dominant electrostatic mechanism. At higher pH, above the pK_a of AY 17, the decrease in the adsorption capacity was lower than acidic pH owing to relatively strong electrostatic interaction than that of other mechanisms such as Lewis-acid-base interaction, London dispersive interaction, and hydrogen bonding that occurred at a higher pH of solution. Unsaturated metals (Perovskite = Fe, Co, and Mn) coordinated with oxygen, carbon (or N) in the DB-perovskite/CAG hybrid can serve as excellent active Lewis-acid sites that can accept and share an electron pair and react with 1 pair of oxygen-containing groups of AY17, thereby forming Lewis acid-base complexes, and successfully led to the adsorption of AY 17 by the DB-perovskite/CAG hybrid. In the DB-perovskite/CAG hybrid, positively charged metals are in fixed positions on the carbon matrix that are surrounded by delocalized electrons.⁶⁴ Thus, the π electrons in the AY17 molecules are accessible to create interactions with the delocalized electrons of the DB-perovskite/CAG hybrid; as a result, the AY 17 molecules are successfully adsorbed on the DB-perovskite/CAG hybrid at higher pH of the solution beside other interaction mechanisms.⁶⁵ Hence, the multitudinous and multifarious active groups and sites of the DB-perovskite/CAG hybrid that confirmed the obtained result allow describing the different magnitude of the interactions between AY17 or CV and DB-perovskite/CAG hybrid as a function of pH.

Adsorption thermodynamics. To understand the adsorption process in terms of feasibility and nature of adsorption, the thermodynamics behavior of the adsorption of both dyes on the DB-perovskite/CAG hybrid was determined at three temperatures (298, 303, and 313 K). The Gibbs free energy (ΔG° , kJ mol⁻¹), enthalpy (ΔH° , kJ mol⁻¹), and entropy (ΔS° , kJ mol⁻¹ K) were obtained using the van't Hoff equation.^{66,67} The thermodynamic parameters were calculated by plotting the graph between $\ln(KT)$ vs. $1/T$, which are depicted in Fig. 7 and Table 2. The adsorption was facilitated at higher temperatures. The rate of diffusion increased at higher temperatures, and the adsorption of both dyes on DB-perovskite/CAG hybrid was an exothermic and spontaneous process. The negative ΔG values at all three temperatures suggested that the adsorption was spontaneous. The ΔG value for both the dyes was reduced with the increase in temperature. At 298 K, the ΔG value for CV was calculated as -0.92 kJ mol⁻¹, which further decreased to -1.94 kJ mol⁻¹ at 313 K. The change in the ΔG value was lower in AY, in which the ΔG value was reduced by 0.89 kJ mol⁻¹ over the same range of temperature by 15°C increase.

Mechanisms of the adsorption process. According to the literature,^{68–71} various mechanisms, namely, hydrogen bonding, pore-filling, van der Waals force, $n-\pi$ interaction, and $\pi-\pi$

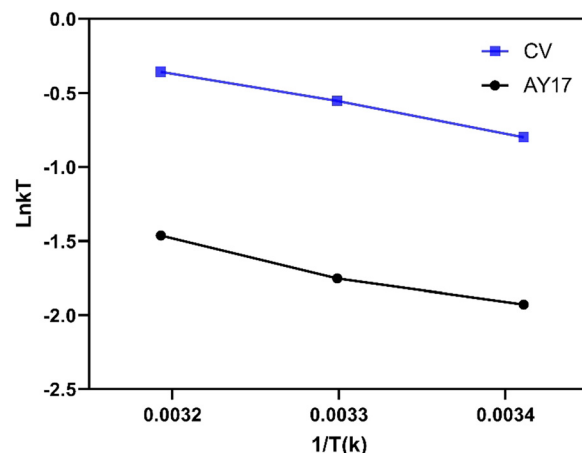
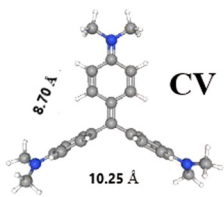



Fig. 7 Van't Hoff plot for the adsorption of CV and AY17 on the DB-perovskite/CAG hybrid pH (neutral); agitation speed (210 rpm); adsorbent dosage (0.1 g for AY17 and 0.05 g for CV); contact time (10 min for CV and 60 min for AY17); initial dye concentration (5–40 mg L⁻¹); and volume of reaction ($V = 50$ mL).

interaction can be considered as the main or secondary adsorption mechanism. Given below is a brief description of the plausible adsorption mechanisms.

Pore filling. The adsorption and desorption isotherms of the CAG and DB-perovskite/CAG hybrid composite under N₂ atmosphere are depicted in Fig. S3 (ESI[†]). The type IV isotherms are shown in CAG curves with an H4 hysteresis loop that is usual for micro and mesoporous compounds. The specific surface area of CAG was 714.9 m² g⁻¹, with a pore volume of 1.1 cm³ g⁻¹, while on introducing DB-perovskite into CAG, a decrease in the specific area and pore volume to 390 m² g⁻¹ and 0.7 cm³ g⁻¹, respectively, were observed. As can be seen, the introduction of Sr_{0.7}Mn_{0.3}Co_{0.5}Fe_{0.5}O_{3- δ} increased the mesostructural properties of CAG. On the other hand, the porosity of CAG after embedding with Sr_{0.7}Mn_{0.3}Co_{0.5}Fe_{0.5}O_{3- δ} improved. The pore size distribution of CAG and DB-perovskite/CAG hybrid composite is depicted in Fig. 8a. CA showed a

Table 2 Thermodynamic parameters for the adsorption process of AY17 and CV on the DB-perovskite/CAG hybrid

Dye	Structure	Temperature (K)	ΔH° (kJ mol ⁻¹)	ΔS° (J mol ⁻¹ K ⁻¹)	ΔG° (kJ mol ⁻¹)
CV		298	-16.87	50.97	-0.92
		303			-1.39
		313			-1.94
AY17		298	-17.73	44.29	-3.80
		303			-4.41
		313			-4.69



bimodal distribution with microspore region, removing these microspores by incorporating $\text{Sr}_{0.7}\text{Mn}_{0.3}\text{Co}_{0.5}\text{Fe}_{0.5}\text{O}_{3-\delta}$ into CAg that generated a single-modal distribution. The obtained parameters from the isotherms and the information in detail are summarized in Tables S5 and S6 (ESI†). The hybrid adsorbent provided great access sites for the adsorption of CV and AY17 because of the existence of many micropores and mesopores, thus improving the adsorption capacity. The average pore size of the DB-perovskite/CAg hybrid composite increased from 6.51 to 24.88 nm due to the removal of micropores. The pore size of the mesopores somehow decreased due to changing the pore size distribution to the large pore size shown in Fig. 8a.

Hydrogen bonding, $n-\pi$ interaction, and $\pi-\pi$ interaction. As shown in Fig. 2, a sharp peak was obtained at nearly 1452 cm^{-1} in the DB-perovskite/CAg hybrid, suggesting the presence of hydroxyl bonding on the surface (M–OH). Both the shifting of the peak and intensity bands also confirmed the interaction between hydroxyl groups and dyes after adsorption occurred. The $\pi-\pi$ stacking interaction is another major mechanism in which sp^2 hybridized C atoms and high chemical/thermal stability of metal oxide materials are involved. A strong interaction would occur between the DB-perovskite/CAg hybrid and the delocalized π bonds of dye molecules.

To provide a better insight into underlying mechanisms in the adsorption of CV and AY17 onto the DB-perovskite/CAg hybrid, the XPS spectra after and before adsorption were recorded. The XPS analysis led to the determination of the surface chemistry and calculated the proportion of oxygen-including functional groups on the surface of the DB-perovskite/CAg hybrid. The C 1s region

curves of the DB-perovskite/CAg hybrid are displayed in Fig. 1b. The main peak at a binding energy (BE) of 283.8 eV was noticed, which could be assigned to the CHx, C–C, and C=C groups of aliphatic and aromatic structures. The two peaks at BE of 286.6 eV and 288.1 eV indicated the presence of C=O in ketone and carbonyl and O–C=O in carboxylic groups, respectively. Also, one more peak at a binding energy of 289.6 eV is assigned to the Plasmon losses or shake-up peak of $\pi-\pi^*$ due to the abundance of π -electrons in the aromatic rings.^{72,73} Three major peaks appeared in the O 1s spectra (Fig. 8b), which were ascribed to C–O–C, –COOH, and C–OH/O–H.⁷⁴ After the adsorption, the interactions occurred between oxygen-containing groups (–O–binds) and CV and AY17 molecules due to the decrease and shifting of the position of the O 1s peaks. Moreover, the new peaks exhibited in the DB-perovskite/CAg hybrid after adsorption suggested the presence of related reactions with CV and AY 17. Thus, it was concluded from the XPS measurement that $\pi-\pi$ stacking or metal– π interactions might have occurred between the positive metal ions and the aromatic ring of CV and AY 17.

Electrostatic interaction. According to the obtained results (Fig. S4, ESI†), the adsorption of CV and AY 17 is primarily governed by the DB-perovskite/CAg hybrid properties, dye structure, and surface charge. The AY17 and CV molecules have a linear and non-linear structure that could be responsible for the adsorption of AY 17 by the porous DB-perovskite/CAg hybrid because the linear molecules could easily penetrate into the DB-perovskite/CAg void spaces. The introduction of $\text{Sr}_{0.7}\text{Mn}_{0.3}\text{Co}_{0.5}\text{Fe}_{0.5}\text{O}_{3-\delta}$ into CAg resulted in surface charge (as observed from zeta potential measurements), revealing an increasing positive charge on the surface

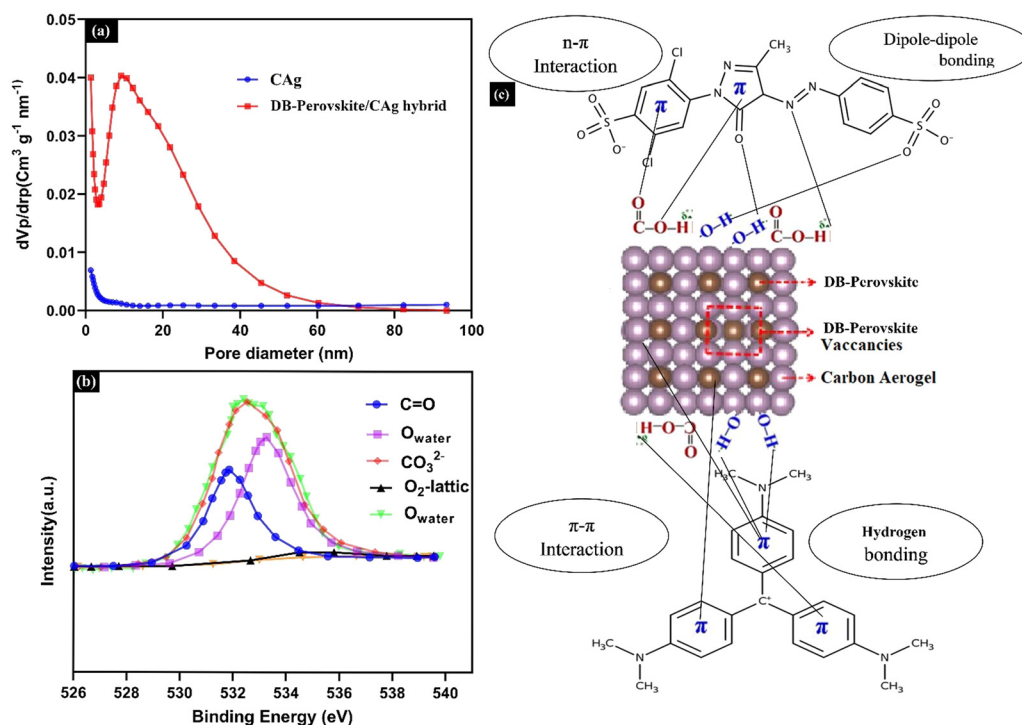


Fig. 8 (a) BJH pore size distribution of CAg and DB-perovskite/CAg hybrid composite; (b) the O 1s spectra of samples obtained from XPS analysis; and (c) illustration of the interaction between AY17 and CV and DB-perovskite/CAg hybrid.



DB-perovskite/CAG Hybrid than that of CAG (from -48.1 mV (CAG) to -24.4 mV). It was thought that the presence of metal oxides on the surface of CAG could increase electrostatic repulsion between the DB-perovskite/CAG hybrid and both dyes.

Hydrophobic interactions. The CAG represents amphipathic characteristics due to the unique properties of organic and inorganic materials ($\text{Sr}_{0.7}\text{Mn}_{0.3}\text{Co}_{0.5}\text{Fe}_{0.5}\text{O}_{3-\delta}$). The presence of oxygen means CAG is polar in nature; therefore, water is adsorbed predominantly. On the surface of the adsorbent, the water are adsorbed *via* hydrogen bonding on oxygen-containing functional groups; in turn, the additional water molecules are clustered at these sites.^{75,76} The hydrophobic nature of CAG causes a decrease in the polar groups in the inner pore structure (active sites of adsorbent). As a result, the accessibility and affinity of the CV and AY17 to the inner pore structure may increase. In turn, the hydrophobic mechanisms might play the main role in CV and AY17 adsorption on the DB-perovskite/CAG hybrid. The proposed mechanisms that could be conceptualized in the adsorption process of AY17 and CV with the DB-perovskite/CAG hybrid composite are given in Fig. 8c.

Atomistic insights into the adsorption process with the DB-perovskite/CAG hybrid. To provide mechanistic information on the adsorption process, DFT calculation was conducted. EXAFS spectra further examined the chemical bonding of the hybrid adsorbent. The CAG surfaces hold polar groups that bond with the oxygen (O site) of $\text{Sr}_{0.7}\text{Mn}_{0.3}\text{Co}_{0.5}\text{Fe}_{0.5}\text{O}_{3-\delta}$. Therefore, the interaction between CAG and $\text{Sr}_{0.7}\text{Mn}_{0.3}\text{Co}_{0.5}\text{Fe}_{0.5}\text{O}_{3-\delta}$ (M)–O–CAG (C) occurs *via* hydrogen bonding, documented by FTIR analysis. This M–O–C bonding causes greater adsorption sites and thus enhances the adsorption of CV and AY17 on the DB-sites perovskite hybrid adsorbent. According to XPS and FTIR analysis, the DB-perovskite/CAG hybrid (are also associated

Table 3 The probable bonding of the DB-perovskite/CAG hybrid

Rank	Bond	d [Å]	d -ratio
1	Fe–O	0.82265	0.43298
2	Fe–O	0.88265	0.43298
3	Fe–O	2.28378	0.43298
4	Fe–O	2.38378	0.43298
5	Co–O	1.06967	0.43298
6	Co–O	1.12856	0.43298
7	Co–O	1.84761	0.43298
8	Co–O	2.41563	0.43298
9	Sr–O	2.28627	0.43298
10	Sr–O	2.34220	0.43298

with double-B-sites perovskite hybrid adsorbent) consists of carbonyl group, hydroxyl groups, and oxygen anions that play major roles to adsorb CV and AY17 besides π – π and electrostatic interactions. As shown in Fig. 9 and Table 3, and Fig. S5 (ESI[†]) (details provided in Tables S7 and S8, ESI[†]), the DB-perovskite/CAG hybrid coordinated with CV and AY17 by oxygen-containing groups and hydrogen atoms. The bond lengths of Fe–O, Co–O, and Sr–O change after doping with Mn. Most Co–O bonds are nearly 1.2 Å with a stable distribution, which decreases to 0.7 Å after doping with Mn. This suggested that the transfer of electron from Co to oxygen or carbon and also the coordination numbers or environments could be enhanced by introducing Mn atoms. This can also be seen for Sr–O bonding, which is more significant. However, the bond lengths of Fe are longer after doping with Mn, and the coordination number of Fe–O increased, demonstrating the effect of Mn atoms on the coordination environments of Fe–Mn. Because of the lower electronegativity of Mn than Fe and Co atoms, Mn atoms could change the valence state and coordination bonds of Fe and Co sites and can cause synergistic impacts on the Fe and Co sites to interact with CV and AY 17. As a result, the higher metal–O bond

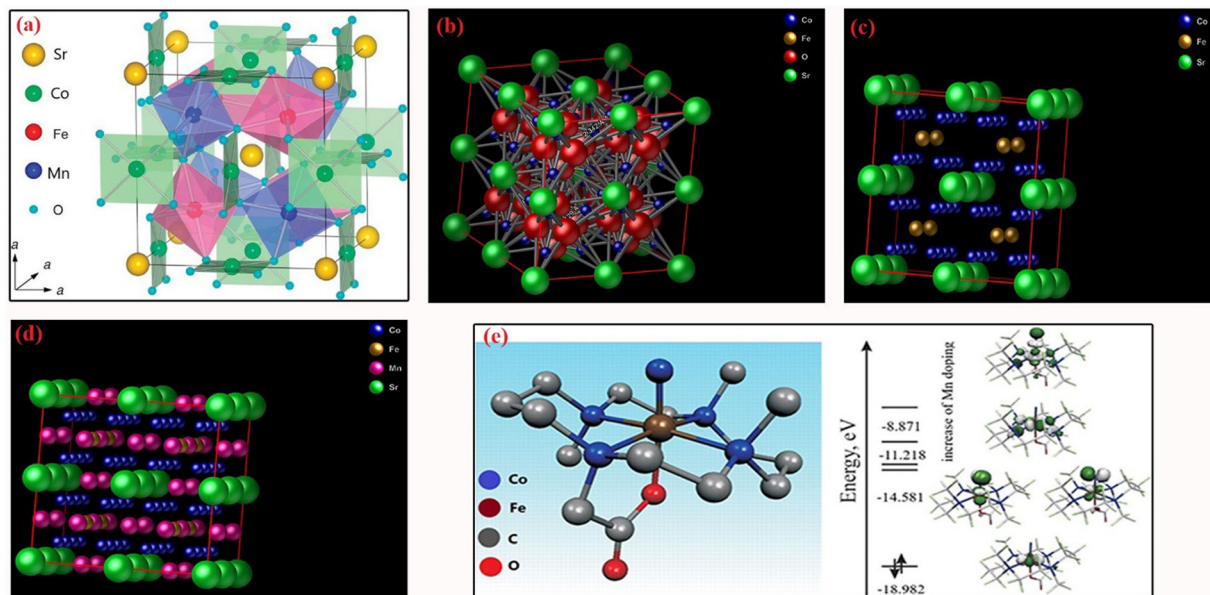


Fig. 9 The DFT-optimized atomic configurations of (a–d) DB-perovskite/CAG hybrid; and (e) free energy diagrams of enhanced CV and AY17 adsorption process by the doping of Mn.



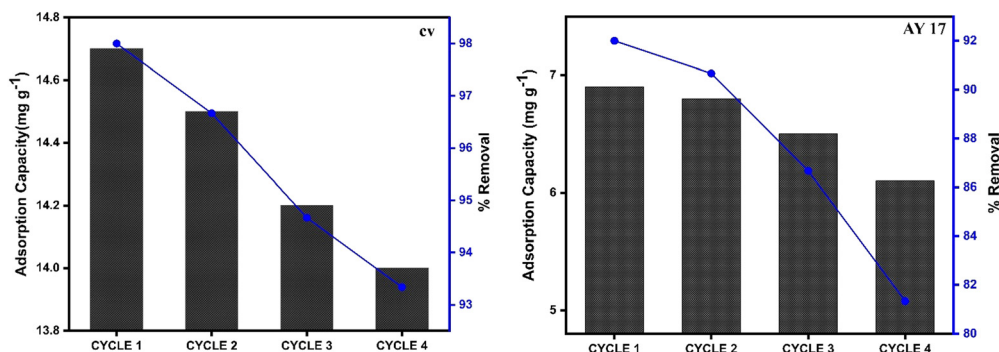


Fig. 10 The adsorption efficiencies and capacity of DB-perovskite/CAG hybrid for AY17 and CV in four adsorption cycles with a pH (neutral); adsorbent dosage (0.1 g for AY17 and 0.05 g for CV); contact time (10 min for CV and 60 min for AY17); initial dyes concentration (5–40 mg L⁻¹); volume of reaction (V = 50 mL); and temperature (25 °C).

strength and the increased Co³⁺/Co²⁺ or Mn⁴⁺/Mn³⁺ ratio enhanced the CV and AY 17 adsorption on the DB-perovskite/CAG hybrid. The adsorption energy of CV and AY17 by DB-perovskite/CAG hybrid was -72.8 and -97.2 kJ mol⁻¹, respectively, showing the exothermic process of adsorption. The doping of Mn exhibits a dramatically smaller adsorption free energy than non-doped DB-perovskite/CAG hybrid, implying the crucial role of Mn-doping in facilitating the CV and AY17 adsorption process.

Desorption and regeneration experiments

The regeneration and reusability of the adsorbent are considered as key characteristics to evaluate the adsorption performance of dyes for field application.^{77–79} Therefore, the regeneration and reusability of CV and AY17 were studied using 0.1 N HCl and 0.1 N HNO₃. After the desorption of dyes from the adsorbent, the regenerated DB-perovskite/CAG hybrid was washed with distilled water and dried in the oven at 50 °C. Then, the reused adsorbent was used for four cycles of desorption–adsorption. As shown in Fig. 10, no remarkable difference was observed between the adsorption–desorption cycles of 0.1 N HCl and 0.1 N HNO₃. As per the results, the regeneration from the first cycle was 98% and 92% for CV and AY17, respectively. After that, the regenerative capacity slightly decreased and reached 93% after four cycles for CV, but the performance of adsorption–desorption for AY17 was significantly reduced to 81%, and decreased sharply with a further increase in the number of cycles. The decrease in AY17 adsorption–desorption performance might be related to net adsorption energy at various contact places between large AY17 molecules and DB-perovskite/CAG hybrid. Moreover, the adsorption capacity of the DB-perovskite/CAG hybrid in the adsorption of CV and AY17 decreased from 14.7 mg g⁻¹ to 14 mg g⁻¹ and 6.9 mg g⁻¹ to 6 mg g⁻¹, respectively, by the end of the 4th regeneration cycle.

Conclusion

A sustainable and efficient DB-perovskiteDB-perovskite (Sr_{0.7}Mn_{0.3}-Co_{0.5}Fe_{0.5}O_{3-δ}) embedded into carbon aerogel (CAG) was successfully synthesized by a pyrolysis method. The applied models indicated that the adsorption of CV and AY17 on the surface of

the DB-perovskite/CAG hybrid was controlled by both external diffusion (film diffusion) and internal diffusion (particle or pore diffusion). The DB-perovskite/CAG hybrid led to a fast and sustainable adsorption capacity for both dyes in a wide range of pH. Thermodynamic analysis showed that the adsorption of CV and AY17 on the DB-perovskite/CAG hybrid is endothermic, indicating that more active sites are available for bonding interactions with the increase in temperature. The higher temperatures increased the static dipole polarizability and promoted the stability of electron acceptors–donors in turn; the interactions between the dyes and functional groups of the DB-perovskite/CAG hybrid were strengthened, indicating increasing weighted mean of site energy distribution at higher temperatures. The Mn atoms exhibited active sites in the DB-perovskite/CAG hybrid due to lower electronegativity than Fe and Mn atoms but still played a critical role in enhancing the valence state of metal ions and strengthened the metals–O bond for the adsorption of CV and AY 17 molecules. DB-perovskite/CAG hybrid acts as a renewable and cost-effective candidate to eliminate cationic and anionic dyes from aqueous solutions because of its higher stability, adsorption capacity, and reusability. Further studies can reveal the application of DB-perovskiteDB-perovskite/CAG hybrid on different dyes and other persistent organic compounds. Another suggestion is the study of the adsorption/desorption cycles and regeneration. This study exhibited that the perovskite-carbon aerogel hybrid adsorbents are competitive for the removal of dyes; the next step is the study of the removal of heavy metals.

Conflicts of interest

There are no conflicts to declare.

References

- 1 J. Gao, Q. Zhang, K. Su, R. Chen and Y. Peng, *J. Hazard. Mater.*, 2010, **174**, 215–225.
- 2 M. Sarmadi, M. Foroughi, H. N. Saleh, D. Sanaci, A. A. Zarei, M. Ghahrchi and E. Bazrafshan, *Environ. Sci. Pollut. Res.*, 2020, 1–17.



- 3 J. Khan, M. Sayed, F. Ali and H. M. Khan, *Z. Phys. Chem.*, 2018, **232**, 507–525.
- 4 W. Ahlawat, N. Kataria, N. Dilbaghi, A. A. Hassan, S. Kumar and K.-H. Kim, *Environ. Res.*, 2020, **181**, 108904.
- 5 J.-M. Yang, R.-J. Ying, C.-X. Han, Q.-T. Hu, H.-M. Xu, J.-H. Li, Q. Wang and W. Zhang, *Dalton Trans.*, 2018, **47**, 3913–3920.
- 6 S. Chang, Q. Zhang, Y. Lu, S. Wu and W. Wang, *Sep. Purif. Technol.*, 2020, **238**, 116400.
- 7 I. Belbachir and B. Makhoukhi, *J. Taiwan Inst. Chem. Eng.*, 2017, **75**, 105–111.
- 8 M. A. Maksoud, R. A. Fahim, A. G. Bedir, A. I. Osman, M. M. Abouelela, G. S. El-Sayyad, M. Abd Elkodous, A. S. Mahmoud, M. M. Rabee and H. Ala'a, *Environ. Chem. Lett.*, 2021, 1–44.
- 9 S. Banerjee, A. Debnath, B. K. Allam and N. Musa, *Environ. Challenges*, 2021, **5**, 100240.
- 10 L. Wang, C. Shi, L. Pan, X. Zhang and J.-J. Zou, *Nanoscale*, 2020, **12**, 4790–4815.
- 11 N. G. Deshpande, C. H. Ahn, D. S. Kim, S. H. Jung, Y. B. Kim and H. K. Cho, *Catal. Sci. Technol.*, 2020, **10**, 6188–6197.
- 12 S. Zhai, R. Chen, J. Liu, J. Xu and H. Jiang, *J. Taiwan Inst. Chem. Eng.*, 2021, **120**, 161–168.
- 13 C. Pei, G. Han, Y. Zhao, H. Zhao, B. Liu, L. Cheng, H. Yang and S. Liu, *J. Hazard. Mater.*, 2016, **318**, 732–741.
- 14 C. B. Njoku, E. Oseghe and T. A. Msagati, *J. Mol. Liq.*, 2022, **346**, 118232.
- 15 X. Li, H. Zhao, J. Liang, Y. Luo, G. Chen, X. Shi, S. Lu, S. Gao, J. Hu and Q. Liu, *J. Mater. Chem. A*, 2021, **9**, 6650–6670.
- 16 X. Ye, X. Wang, Z. Liu, B. Zhou, L. Zhou, H. Deng and Y. Long, *Dalton Trans.*, 2022, **51**, 1745–1753.
- 17 H. Wang, Q. Zhang, M. Qiu and B. Hu, *J. Mol. Liq.*, 2021, **334**, 116029.
- 18 É. Nascimento, A. Garrido Pedrosa and M. Souza, *Water Sci. Technol.*, 2021, **83**, 2793–2808.
- 19 K. Gupta, P. Joshi, R. Gusain and O. P. Khatri, *Coord. Chem. Rev.*, 2021, **445**, 214100.
- 20 A. Ruhaimi, M. Aziz and A. Jalil, *J. CO₂ Util.*, 2020, 101357.
- 21 R. A. Gopal, M. Song, D. Yang, T. Lkhagvaa, S. Chandrasekaran and D. Choi, *Environ. Pollut.*, 2020, **267**, 115498.
- 22 Y. Jiang, Q. Shen, S. Li, G. Yang and N. Huang, *New J. Chem.*, 2020, **44**, 6003–6009.
- 23 H. Sun, G. Chen, Y. Zhu, B. Liu, W. Zhou and Z. Shao, *Chem. – Eur. J.*, 2017, **23**, 5722–5728.
- 24 H. Mersian and M. Alizadeh, *Ceram. Int.*, 2020, **46**, 17197–17208.
- 25 B. C. Mastoroudes, J. Markgraaff, J. B. Wagener and E. J. Olivier, *Chem. Phys.*, 2020, **537**, 110816.
- 26 N. Choudhary, M. K. Verma, N. D. Sharma, S. Sharma and D. Singh, *Mater. Chem. Phys.*, 2020, **242**, 122482.
- 27 A. H. Mahvi, M. Sarmadi, D. Sanaei and H. Abdolmaleki, *Desalin. Water Treat.*, 2020, **200**, 205–216.
- 28 M. H. Dehghani, M. Sarmadi, M. R. Alipour, D. Sanaei, H. Abdolmaleki, S. Agarwal and V. K. Gupta, *Microchem. J.*, 2019, **146**, 1043–1053.
- 29 B. B. Mohammed, A. Hsini, Y. Abdellaoui, H. Abou Oualid, M. Laabd, M. El Ouardi, A. A. Addi, K. Yamni and N. Tijani, *J. Environ. Chem. Eng.*, 2020, **8**, 104419.
- 30 M. H. Dehghani, D. Sanaei, I. Ali and A. Bhatnagar, *J. Mol. Liq.*, 2016, **215**, 671–679.
- 31 P. Song, B. Liu, C. Liang, K. Ruan, H. Qiu, Z. Ma, Y. Guo and J. Gu, *Nano-Micro Lett.*, 2021, **13**, 1–17.
- 32 C. Duan, T. Ma, J. Wang and Y. Zhou, *J. Water Process Eng.*, 2020, **37**, 101339.
- 33 J. Liu, X. Yang, H. Liu, W. Cheng and Y. Bao, *Colloids Surf., A*, 2020, **601**, 124960.
- 34 S. Sun, Z. Yang, J. Cao, Y. Wang and W. Xiong, *J. Solid State Chem.*, 2020, **285**, 121219.
- 35 Y. Gao, R. Kang, J. Xia, G. Yu and S. Deng, *J. Colloid Interface Sci.*, 2019, **535**, 159–168.
- 36 M. A. Al-Ghouti and D. A. Da'ana, *J. Hazard. Mater.*, 2020, **393**, 122383.
- 37 Q. T. N. Le and K. Cho, *J. Colloid Interface Sci.*, 2021, **581**, 741–750.
- 38 D. Panchal, A. Sharma, P. Mondal, O. Prakash and S. Pal, *Appl. Surf. Sci.*, 2021, **553**, 149577.
- 39 M. T. Amin, A. A. Alazba and M. Shafiq, *Sustainability*, 2021, **13**, 3600.
- 40 A. A. Khan, A. Molla, A. Chowdhury, S. Kumari and S. Hussain, *ACS Appl. Nano Mater.*, 2021, **4**, 4114–4128.
- 41 S. Wong, H. H. Tumari, N. Ngadi, N. B. Mohamed, O. Hassan, R. Mat and N. A. S. Amin, *J. Cleaner Prod.*, 2019, **206**, 394–406.
- 42 S. Wong, N. Abd Ghafar, N. Ngadi, F. A. Razmi, I. M. Inuwa, R. Mat and N. A. S. Amin, *Sci. Rep.*, 2020, **10**, 1–13.
- 43 M. Zbair, Z. Anfar, H. A. Ahsaine, N. El Alem and M. Ezahri, *J. Environ. Manage.*, 2018, **206**, 383–397.
- 44 M. Massoudinejad, H. Rasoulzadeh and M. Ghaderpoori, *Carbohydr. Polym.*, 2019, **206**, 844–853.
- 45 L. M. Silva, M. J. Muñoz-Peña, J. R. Domínguez-Vargas, T. González and E. M. Cuerda-Correa, *Surf. Interfaces*, 2021, **22**, 100791.
- 46 R. Leyva-Ramos, J. Salazar-Rábago and R. Ocampo-Pérez, *Chem. Eng. Res. Des.*, 2021, **172**, 43–52.
- 47 G. Bufalo, F. Di Nezza, M. Perna, S. Salvestrini and L. Ambrosone, *Appl. Sci.*, 2021, **11**, 3096.
- 48 J.-J. Lee, *Clean Technol.*, 2021, **27**, 182–189.
- 49 K. A. M. Said, A. Ismail, A. Zulhairun, M. Abdullah, J. Usman, M. A. Azali and M. A. Azali, *J. Environ. Chem. Eng.*, 2021, **9**, 105036.
- 50 H. Feng, Z. Feng, W. Wang, Z. Deng and B. Zheng, *Constr. Build. Mater.*, 2021, **292**, 123285.
- 51 H. Lei, Y. Muhammad, K. Wang, M. Yi, C. He, Y. Wei and T. Fujita, *J. Hazard. Mater.*, 2021, **406**, 124292.
- 52 F. M. Mpatani, R. Han, A. A. Aryee, A. N. Kani, Z. Li and L. Qu, *Sci. Total Environ.*, 2021, 146629.
- 53 V. Inglezakis, M. Fyrillas and J. Park, *J. Hazard. Mater.*, 2019, **367**, 224–245.
- 54 A. Z. Baimenov, D. Berillo, K. Moustakas and V. Inglezakis, *J. Hazard. Mater.*, 2020, **399**, 123056.
- 55 E. Q. Adams and L. Rosenstein, *J. Am. Chem. Soc.*, 1914, **36**, 1452–1473.
- 56 D. Brunel and F. Dumur, *New J. Chem.*, 2020, **44**, 3546–3561.
- 57 D. R. Waring and G. Hallas, *The chemistry and application of dyes*, Springer Science & Business Media, 2013.



- 58 P. F. Gordon and P. Gregory, *Organic chemistry in colour*, De Gruyter, 2022.
- 59 H. Shindy, *Dyes Pigment.*, 2017, **145**, 505–513.
- 60 M. Teli and G. T. Nadathur, *J. Environ. Chem. Eng.*, 2018, **6**, 7257–7272.
- 61 M. Pérez-Urquiza and J. Beltrán, *J. Chromatogr. A*, 2001, **917**, 331–336.
- 62 J.-F. Gao, Q. Zhang, K. Su and J.-H. Wang, *Bioresour. Technol.*, 2010, **101**, 5793–5801.
- 63 R. Srinivasan, M. N. Kathiravan and K. P. Gopinath, *Bioresour. Technol.*, 2011, **102**, 2242–2247.
- 64 S. Parvez, M. J. Long, J. R. Poganik and Y. Aye, *Chem. Rev.*, 2018, **118**, 8798–8888.
- 65 S. Shakra, H. Hanna and A. Hebeish, *Angew. Makromol. Chem.*, 1979, **75**, 53–62.
- 66 D. O. Omokpariola, *J. Chem. Lett.*, 2021, **2**, 9–24.
- 67 B. Priyadarshini, T. Patra and T. R. Sahoo, *J. Magnesium Alloys*, 2021, **9**, 478–488.
- 68 J. Zhao, C. Wang, S. Wang and Y. Zhou, *J. Ind. Eng. Chem.*, 2020, **83**, 111–122.
- 69 S. Shang, Y. Liu, M. Liu, Y. Bai, X. Wang, B. Wu, J. Chen, J. Dong and Y. Liu, *J. Hazard. Mater.*, 2022, **421**, 126796.
- 70 H. Rasoulzadeh, A. Sheikhmohammadi, M. Abtahi, B. Roshan and R. Jokar, *J. Environ. Chem. Eng.*, 2021, **9**, 105954.
- 71 H. Rasoulzadeh, A. Sheikhmohammadi, M. Abtahi, M. Alipour and B. Roshan, *Int. J. Environ. Anal. Chem.*, 2021, 1–14.
- 72 L. Zhang, Y. Liu, Y. Wang, X. Li and Y. Wang, *Appl. Surf. Sci.*, 2021, **557**, 149838.
- 73 S. Hussain, M. Kamran, S. A. Khan, K. Shaheen, Z. Shah, H. Suo, Q. Khan, A. B. Shah, W. U. Rehman and Y. O. Al-Ghamdi, *Int. J. Biol. Macromol.*, 2021, **168**, 383–394.
- 74 Y. Tanimoto and S.-I. Noro, *RSC Adv.*, 2021, **11**, 23707–23713.
- 75 K. Belkassa, M. Khelifa, I. Batonneau-Gener, K. Marouf-Khelifa and A. Khelifa, *J. Hazard. Mater.*, 2021, **415**, 125656.
- 76 I. V. Melnyk, V. V. Tomina, N. V. Stolyarchuk, G. A. Seisenbaeva and V. G. Kessler, *J. Mol. Liq.*, 2021, **336**, 116301.
- 77 N. S. A. Mubarak, T. Chuan, H. Khor, A. H. Jawad, L. Wilson and S. Sabar, *J. Polym. Environ.*, 2021, **29**, 1050–1062.
- 78 J. Zhou, Y. Zhang, G. Jia, Z. Chen, Y. Yang and L. Zhang, *New J. Chem.*, 2021, **45**, 4835–4842.
- 79 B. F. do Nascimento, C. M. B. de Araujo, A. C. do Nascimento, G. R. B. da Costa, B. F. M. L. Gomes, M. P. da Silva, R. K. da Silva Santos and M. A. da Motta Sobrinho, *Bioresour. Technol. Rep.*, 2021, 100767.

